

Atomic arrangements in an amorphous CoFeB ribbon extracted via an analysis of radial distribution functions

Pussi K., Barbiellini B., Ohara K., Yamada H., Dwivedi J., Bansil A., Gupta A., Kamali S.

This is a Post-print version of a publication
published by IOP Publishing
in Journal of Physics: Condensed Matter

DOI: 10.1088/1361-648X/ac1238

Copyright of the original publication:

© 2021 IOP Publishing

Please cite the publication as follows:

Pussi, K., Barbiellini, B., Ohara, K., Yamada, H., Dwivedi, J., Bansil, A., Gupta, A., Kamali, S. (2021). Atomic arrangements in an amorphous CoFeB ribbon extracted via an analysis of radial distribution functions. *Journal of Physics: Condensed Matter*, vol. 33, issue 39. DOI: 10.1088/1361-648X/ac1238

**This is a parallel published version of an original publication.
This version can differ from the original published article.**

Atomic arrangements in an amorphous CoFeB ribbon extracted via an analysis of radial distribution functions

K. Pussi* and B. Barbiellini†

Physics Department, School of Engineering Science, LUT University, 53851 Lappeenranta, Finland

K. Ohara and H. Yamada

*Japan Synchrotron Radiation Research Institute, SPring-8,
1-1-1 Kouto, Sayo-cho, Sayo-gun, Hyogo 679-5198 Japan*

J. Dwivedi

School of Physics, Devi Ahilya University, Indore 452001, India

A. Bansil

Physics Department, Northeastern University, Boston, MA 02115, United States

A. Gupta

Department of Physics, University of Petroleum and Energy Studies, Bidholi, Dehradun- 248007, India

S. Kamali‡

*Department of Mechanical, Aerospace and Biomedical Engineering,
University of Tennessee Space Institute, Tullahoma, TN 37388 United States and
Department of Physics and Astronomy, Middle Tennessee State University, Murfreesboro, TN 37132, United States
(Dated: August 22, 2021)*

We discuss the atomic structure of amorphous ferromagnetic FeCoB alloys, which are used widely in spintronics applications. Specifically, we obtain the pair-distribution functions for various atomic pairs based on high-energy x-ray diffraction data taken from an amorphous $\text{Co}_{20}\text{Fe}_{61}\text{B}_{19}$ specimen. We start our reverse Monte Carlo cycles to determine the disordered structure with a two-phase model in which a small amount of cobalt is mixed with Fe_{23}B_6 as a second phase. The structure of the alloy is found to be heterogeneous, where the boron atoms drive disorder through the random occupation of the atomic network. Our analysis also indicates the presence of small cobalt clusters that are embedded in the iron matrix and percolating the latter throughout the structure. This morphology can explain the enhanced spin polarization observed in amorphous magnetic materials.

I. INTRODUCTION

Two-dimensional (2D) structures in the form of thin films, multilayers, and superlattices are an important class of nanomaterials, which can host structural and magnetic properties that are not found in their bulk counterparts [1, 2]. Properties of nanostructures are also amenable to being tailored, making them suitable as platforms for applications such as the magnetoresistive random access memory [3] based on the Magnetic Tunnel Junction (MTJ) [4–8]. Interfaces play a key role and the presence of roughness and steps dictate their physical properties. A large number of studies in MTJs, for example, investigate effects of parameters such as post-annealing [9–11], oxidation conditions [12, 13], Boron-enrichment [14, 15], and the capping layers [16] to achieve higher tunnel magnetoresistance values.

Nanoglasses, which represent a novel structural modification of amorphous materials, exhibit internal structural features on length scale of a few nanometers that result in significant changes in the density and chemical composition [17]. Considerable experimental and theoretical (computer simulations) effort has been made over the last few decades to explore atomic configurations in metallic glasses, and yielded a number of structural models, which successfully describe characteristics of metallic glasses from various perspectives [18–20]. Amorphous materials have also been used as building blocks in thin films and multilayers, where they provide soft magnetic properties, low coercivity, and high saturation magnetization as well as control of electron and mass densities.

Our recent studies of nanoglasses using synchrotron-based techniques (high-energy x-ray diffraction (HE-XRD) and magnetic Compton scattering) have revealed interesting structural and magnetic properties such as the existence of interfaces in compacted nanoparticle materials, short-range order (SRO) with an enhanced free volume [21], as well as an itinerant low-temperature component in the magnetism of FeSc nanoglasses [22]. Here, we apply HE-XRD measurements combined with the determination of the atomic

* katiina.pussi@lut.fi

† Also at: Physics Department, Northeastern University, Boston, MA 02115, United States

‡ skamalim@utk.edu

pair-distribution functions (PDFs) [23] to unravel the structure of amorphous FeCoB alloys, which are a key component of the MTJs. Specifically, we investigate a $\text{Co}_{20}\text{Fe}_{61}\text{B}_{19}$ alloy sample.

The first step involves obtaining the total structure factor, also called the Faber-Ziman total structure factor [24], $S(Q)$, which is a function of the absolute wave number Q ($Q = |\mathbf{Q}| = (4\pi/\lambda)\sin\theta$), where λ is the wavelength of the incident x-rays and θ is the scattering angle. The $S(Q)$ is related to the coherent part ($I^{\text{coh}}(Q)$) of the diffraction data [25] as follows:

$$S(Q) = 1 + \frac{I^{\text{coh}}(Q) - \sum C_i |f_i(Q)|^2}{|\sum C_i f_i(Q)|^2}, \quad (1)$$

where $f_i(Q)$ is the atomic scattering factor and C_i is the atomic concentration of species of type i . The reduced PDF, denoted $G(r)$, is given by the Fourier transform of $Q[S(Q) - 1]$:

$$G(r) = \frac{2}{\pi} \int_{Q_{\min}}^{Q_{\max}} Q[S(Q) - 1] \sin(Qr) dQ, \quad (2)$$

and it is defined by the formula

$$G(r) = 4\pi r[(\rho(r) - \rho_0)], \quad (3)$$

where ρ_0 is the atomic number density and $\rho(r) = \rho_0 g(r)$ is the atomic pair density proportional to the PDF, $g(r)$. The peaks of $G(r)$ and $g(r)$ are associated with preferred atomic distances in the structure. Note that in order to improve spatial resolution of $G(r)$, $S(Q)$ must be measured with a higher Q cut-off Q_{\max} , which becomes possible due to the higher photon energies available in the HE-XRD technique. The radial distribution function (RDF) is obtained from $g(r)$ as [26]:

$$RDF(r) = 4\pi r^2 \rho_0 g(r). \quad (4)$$

The PDF approach has been shown to be a useful method for determining the structures of non-crystalline and disordered materials as well as nanoparticles [25, 27–48].

II. EXPERIMENTAL DETAILS

Our amorphous alloy sample was in the form of a 1 cm wide ribbon with nominal composition of $\text{Co}_{20}\text{Fe}_{61}\text{B}_{19}$. It was prepared via the planar flow-casting technique [49]. HE-XRD measurements were performed with a photon wavelength of 0.21 Å in the transmission mode at beamline BL04B2 of the Japanese synchrotron facility SPring-8. An ionization chamber was used for monitoring the intensity of incident x-rays, while three CdTe detectors were used for monitoring the intensity of the scattered x-rays. Furthermore, a two-axis diffractometer installed at BL04B2 can cover low- Q region ($\approx 0.1 \text{ \AA}^{-1}$). Our setup for the HE-XRD beamline is described in detail elsewhere [50]. In order to achieve high real-space

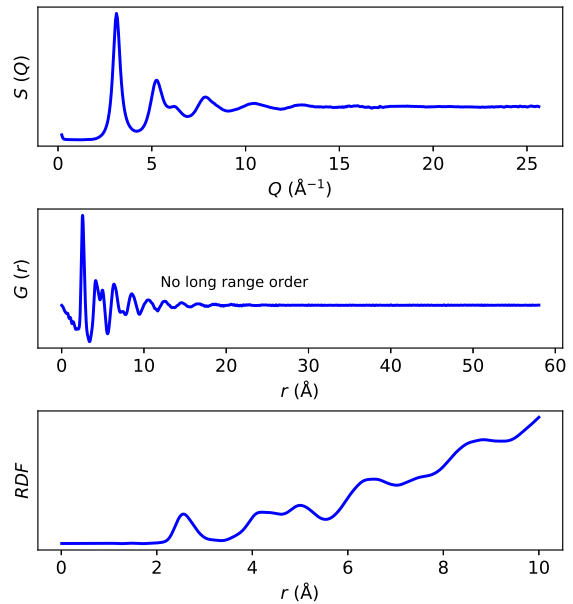


FIG. 1. From top to bottom: The total structure factor, $S(Q)$, the reduced pair distribution function, $G(r)$, and the radial distribution function, RDF, for the investigated $\text{Co}_{20}\text{Fe}_{61}\text{B}_{19}$ sample.

resolution, the full 2θ range was used to model the structure factor up to 25.6 \AA^{-1} . The results of the analysis are shown in Figure 1.

It is interesting to compare our results with those obtained by Quirinale [51] for the structure of liquid $\text{Fe}_{83}\text{B}_{17}$ using HE-XRD and neutron diffraction. A predominance of icosahedral ordering is found in liquid $\text{Fe}_{83}\text{B}_{17}$, which is consistent with the well-known glass-formability of the Fe-B system and the features observed in the $S(Q)$ data [51]. The main features of our $S(Q)$ and $G(r)$ data on Fe_{23}B_6 , shown in Figure 1, are similar to the corresponding results of Quirinale [51]. However, there also are significant differences that come from the fact that Quirinale’s sample is liquid, while in our case we have an amorphous solid. For example, in our $S(Q)$, the second peak has a noticeable shoulder on the high-momentum side, which is not present in Quirinale’s data. Similarly, the second peak of our $G(r)$ is a double peak, while Quirinale has a wide single peak. The appearance of the sub-peak structure in our second $G(r)$ peak indicates local ordering tendency in the amorphous sample. In our case, the first peak in the PDF, which denotes the most probable nearest-neighbor distance in the structure, is centered at 2.55 \AA and lies close to bulk bond length of Fe (2.482 \AA) and Co (2.506 \AA). It should be noted [52] that structural relaxation is not an incipient crystallization process, but that it is a transformation toward a more stable amorphous state driven by collective atomic motions of structural defects in which the nearest-neighbor distances and coordination numbers stay basically unchanged.

Wyckoff class	Fractional coordinates (x, y, z)	Sites in the unit cell (%)
24e	0.2765, 0, 0	20.69
8c	0.25, 0.25, 0.25	6.89
4a	0, 0, 0	3.45
32f	0.3809, 0.3809, 0.3809	27.59
48h	0, 0.1699, 0.1699	41.38

TABLE I. Site occupations in the Fe_{23}B_6 structure. B atoms occupy the 24e site and Fe atoms occupy the 8c, 4a, 32f, and 48h sites.

III. RESULTS AND DISCUSSION

In order to reconstruct the atomic arrangements from the HE-XRD data, we used two different software packages. DiffPy-CMI [53], which is a Python-based code for modeling crystalline and amorphous nano-systems, was used for an initial screening of possible structures. This was followed by a more detailed analysis using the RMCProfile [54] code, which is based on a Reverse Monte Carlo (RMC) method for crystalline and disordered materials. Since our sample is amorphous, calculations in real space were mostly limited to the range of 0-10 Å. Above 10 Å, the $G(r)$ starts to decay and it approaches zero as illustrated in Figure 1. The RMC strategy is particularly suited for modeling amorphous materials since the PDF here consists of only a few peaks or prominent features even though the number of refined parameters in the model involves several thousand atomic coordinates. For these reasons, a careful choice of constraints is essential for obtaining a reasonable structural model. These constraints should also be kept in mind in interpreting the final structural model [55].

Diffpy-CMI [53] was used to obtain PDFs for a selected set of periodic model structures. Since amorphous materials often show features of crystalline phases (e.g. SRO similar to that found in the known crystallographic structures of related compounds) [55], this analysis was started with Fe_{23}B_6 , which adopts the Cr_{23}C_6 prototype structure. Cr_{23}C_6 has a large unit cell of more than 1 nm size, containing 92 medium-sized ferromagnetic transition-metal (TM) elements and 24 small metalloid atoms. The unit cell parameter of Fe_{23}B_6 is $a = 10.607$ Å. B atoms occupy the 24e sites of the $Fm-3m$ space group and Fe atoms occupy the 8c, 4a, 32f, and 48h sites. Fe-Fe bond lengths range between 2.41-2.90 Å, and the Fe-B bond lengths are 2.10 and 2.13 Å. Notably, the Fe_{23}B_6 phase is a metastable phase, which can easily decompose into Fe_3B and $\alpha\text{-Fe}$, although it can be stabilized if the Fe atom is partially substituted by another TM atom [56–58]. Table I summarizes the site occupations in the Fe_{23}B_6 structure.

Simple models based on Fe_{23}B_6 gave reasonable agreement with the experimental PDF, but important details, such as the sub-peak structure of the second $G(r)$ peak, were not reproduced. Since our sample, $\text{Co}_{20}\text{Fe}_{61}\text{B}_{19}$, has Co, some Co was introduced into the Fe_{23}B_6 lattice in order to achieve our experimental stoichiometry. Co atoms cannot be incorporated interstitially nor can they substitute for B atoms. Co could however be substituted on Fe 4a, 8c,

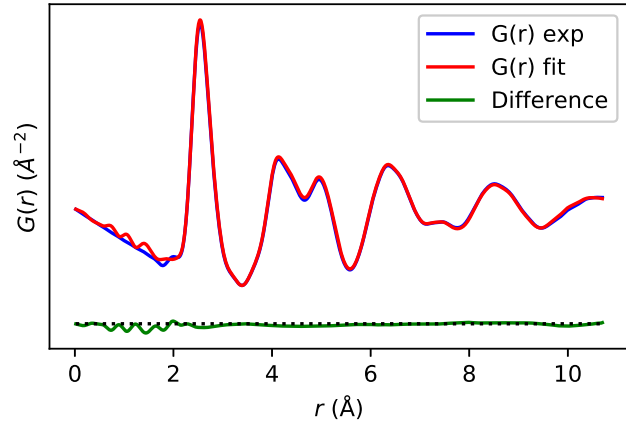
32f, or 48h Wyckoff sites. Out of these, the 8c site is the most spacious one with distances to its nearest-neighbor 32f and 48h sites of 2.41 Å and 2.90 Å, respectively. The Co substitution was tried for various Fe sites, but none of the tested structures significantly improved the agreement with experiment compared to the pristine Fe_{23}B_6 structure.

The experimental PDF was then modeled using a two-phase approach in which a small amount of Co PDF was mixed with the Fe_{23}B_6 PDF as a second phase. Also a lower-symmetry periodic model structure, $P6_3/mmc$, was introduced for Fe_{23}B_6 , which supports a more versatile setting of bond lengths compared to the $Fm-3m$ structure. Overall, the two-phase approach brought some improvement to the fit compared to the case of ordered Co inclusions, but we were still not fully able to reproduce the important sub-peak structure of the second $G(r)$ peak. Partial Co occupation was also tried using various Fe sites in the lattice (i.e. each Fe site in the lattice is occupied by $0.26 \times \text{Co} + 0.74 \times \text{Fe}$). These results also did not show much difference compared to ordered Co in the Fe_{23}B_6 lattice.

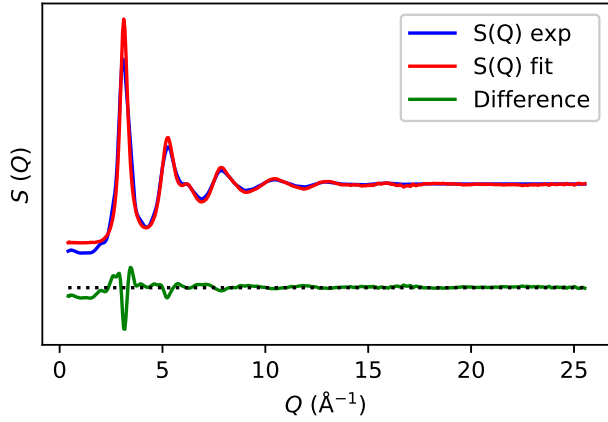
Since the Diffpy-CMI [53] results were not conclusive, we turned to investigate the effect of adding Co randomly into the Fe_{23}B_6 structure. This was done with RMCProfile [54] using cluster models. RMCProfile can fit the total scattering data in either the reciprocal or the real space, i.e. the total scattering structure factors or the PDFs. The experimental data can be used thus in two different ways, which is beneficial since the real and reciprocal space functions emphasize different aspects of the structure. The PDF highlights the structure at short distances, whereas the scattering data are weighted in favor of the longer-range structure. Since our sample is amorphous and we do not expect to see much long-range order, we focus more on the PDF in our analysis.

The starting structure in the calculations was an $8 \times 8 \times 8$ unit cell of the ideal Fe_{23}B_6 lattice, with a cube side of 86 Å that contains a total of 59,392 atoms. 74% of the original Fe sites were occupied randomly by the Fe atoms, while the remaining 26% sites were occupied randomly by Co atoms, giving a stoichiometry close to that of our sample ($\text{Co}_{20}\text{Fe}_{61}\text{B}_{19}$). In the structure refinement, the Co and Fe atoms were allowed to swap. Some constraints/restraints were included in the calculations in order to keep the structure physically sound. The PDF of the optimized structure in Figure 2(a) shows excellent agreement with experiment. The fitted reciprocal-space data is shown in Figure 2(b). We have used a Fourier filter to remove spurious features at short distances in the experimental $G(r)$. Discrepancies in $S(Q)$ between the experimental and simulated results in the low- Q region reflect the uncertainties inherent in our modeling amorphous structures at large distances.

The RMCProfile [54] optimized computational cell is shown in Figure 3. This structure is consistent with the density-functional theory results of Paluskar *et al.* [59]. The Co atoms (green balls) tend to occur in the form of



(a)



(b)

FIG. 2. The theoretical (a) $G(r)$ and (b) $S(Q)$ data fitted to the corresponding experimental results from $\text{Co}_{20}\text{Fe}_{61}\text{B}_{19}$.

small clusters as highlighted in Figure 4, which shows a $16 \text{ \AA} \times 16 \text{ \AA} \times 16 \text{ \AA}$ cube cut from the center of the full calculation cell of Figure 3. The Co-clustering obtained via RMCProfile [54] modeling is consistent with our Diffpy-CMI [53] results, which indicates that it is better to include cobalt as a second phase in the calculations, rather than as ordered Fe sites or partial Co occupancy.

We note that our $G(r)$ results are in good agreement with those of Kirk *et al.* [60] obtained from amorphous CoFeB thin films using electron-diffraction data. The first $G(r)$ peak in Figure 2(a), which is centered at 2.55 \AA and seen to be relatively sharp, is mainly contributed by the TM-TM bonds and corresponds to the TM-TM distance. The small shoulder around 2 \AA comes from TM-B bonds. The second double-peak is wide and it forms as a result of hybridization of various bonds. The SRO is thus dominated by clusters consisting of TM-TM and TM-B bonds with lengths ranging from $2\text{-}3 \text{ \AA}$. These clusters then connect and even overlap with each other throughout the glassy matrix to form a variety of atomic configurations beyond the nearest-neighbour shell

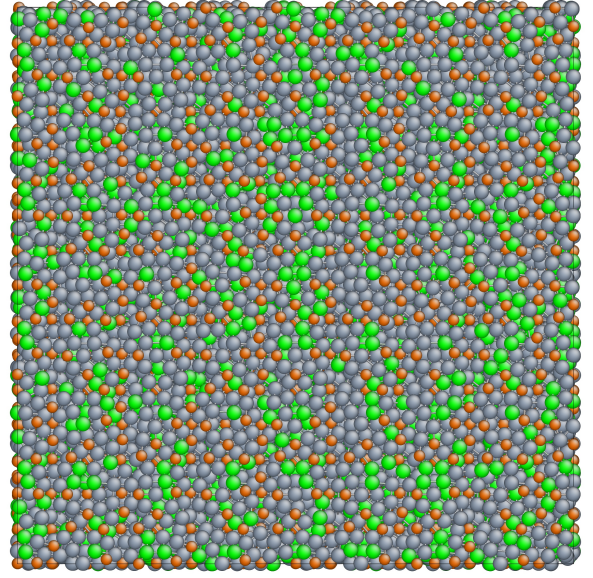


FIG. 3. Optimized geometry of the computational cell. The figure shows atomic positions on one side of our $86 \text{ \AA} \times 86 \text{ \AA} \times 86 \text{ \AA}$ cube. Green atoms are Co, grey atoms are Fe, and brown atoms are B.

on a scale extending from a few to about 10 \AA [61].

Following a fit to the experimental radial distribution function, we obtain the average TM-TM and TM-B distances of $2.55 \pm 0.02 \text{ \AA}$ and $2.00 \pm 0.02 \text{ \AA}$, respectively. The standard deviations here reflect effects of distance distributions and distortions of the local structure in the amorphous structure. Our error bars are comparable to those reported by Kirk *et al.* [60]. B-B bonds were not observed in the model. However, due to the small relative contribution to the total scattering by B atoms, the RMC refinements alone cannot be relied upon to confirm or reject the formation of B-B bonds [60].

The partial PDFs for the optimized structure are shown in Figure 5. These results agrees with those shown in Fig. 2 of the paper by Paluskar *et al.* [59]. Beyond the first peak, the partial PDFs show relatively wide peaks for Fe-Fe, Fe-Co, and Co-Co pairs. The B-B partial PDF has narrower peaks. The width of a peak depends on the distribution of distances around the average value due to thermal vibrations and structural disorder. For a completely random distribution, the PDF will be flat and equal to 0 for any value of r .

As we noted already, amorphous CoFeB alloys have been deployed as ferromagnetic electrodes in MTJs due to their high magnetoresistance [59, 62, 63]. The intrinsic spin polarization values decrease with increasing Co content, but still stay substantially larger than the values in common magnetic metals such as Fe, Co, and Ni [62]. This can be understood to be the result of Co clustering, which induces a reduction in the magnetostrictive properties with increasing Co content [63]. Because our sample is Fe rich, the Fe

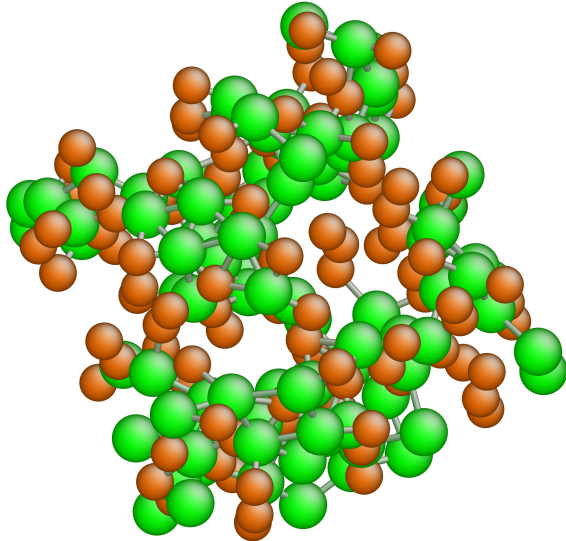


FIG. 4. Clustering of the Co atoms. The figure shows a small portion taken from inside our computational cell, shown in Figure 3, over the fractional range $[x=y=z_{min}=0.4; x=y=z_{max}=0.6]$, near the center of the cube. Green atoms are Co and brown atoms are B. Fe atoms are not shown for clarity.

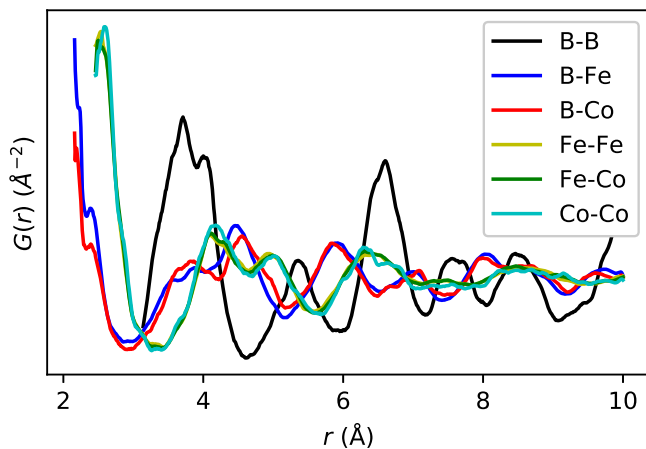


FIG. 5. Partial pair-distribution functions for the optimized geometry.

matrix can still percolate throughout the sample despite the

clustering of Co. This percolation property of Fe is important for the presence of itinerant magnetism in the sample [64], while localized moments can build up in the Co clusters shown in Figure 4.

The atomic distribution shown in Figure 4 is consistent with the results of Huang *et al.* [62] and Diaz *et al.* [63], who demonstrate that FeCoB alloys are heterogeneous and that their magnetostrictive properties originate in the random distribution of B atoms. Further support for the importance of B disorder is given by Paluskar *et al.* [59], who report first-principles atomic and electronic structures that reveal striking agreement between the measured and predicted tunneling spin polarization and demonstrate that B contributes to the spin polarization in FeCoB alloys.

IV. CONCLUSION

The large momentum range accessible via high-energy x-rays at synchrotron radiation facilities enables experiments for probing short-range ordering in complex materials [65]. The combination of total scattering measurements with reverse Monte Carlo modeling is an effective tool for investigating structures of amorphous and disordered crystalline materials [66]. We deploy this approach to uncover the atomic structure of amorphous CoFeB alloys with high accuracy. The presence of Co nanoclusters in the structure enhances spin polarization [59, 62] through an intricate interplay involving itinerant $3d$ electrons in the Fe matrix and the localized magnetic moments on Co nanoclusters. Our study thus highlights the importance of heterogeneity [67] in the functional properties of spintronics materials.

ACKNOWLEDGMENTS

The work at LUT university was supported by the Academy of Finland grant number 326325. The authors wish to acknowledge CSC-IT Center for Science, Finland, for computational resources. The work at Northeastern University was supported by the US Department of Energy (DOE), Office of Science, Basic Energy Sciences grant number DE-FG02-07ER46352, and benefited from Northeastern University's Advanced Scientific Computation Center (ASCC) and the NERSC supercomputing center through DOE grant number DE-AC02-05CH11231. The HE-XRD experiments were performed with the approval of the Japan Synchrotron Radiation Research Institute (Proposal No.: 2020A1238).

[1] A. Sáenz-Trevizo and A. Hodge, *Nanotechnology* **31**, 292002 (2020).

[2] B. Dieny, I. L. Prejbeanu, K. Garello, P. Gambardella, P. Freitas, R. Lehndorff, W. Raberg, U. Ebels, S. O. Demokritov, J. Akerman, *et al.*, *Nature Electronics* **3**, 446 (2020).

- [3] J. Åkerman, *Science* **308**, 508 (2005).
- [4] T. Miyazaki and N. Tezuka, *Journal of Magnetism and Magnetic Materials* **139**, L231 (1995).
- [5] J. S. Moodera, L. R. Kinder, T. M. Wong, and R. Meservey, *Phys. Rev. Lett.* **74**, 3273 (1995).
- [6] S. Ikeda, K. Miura, H. Yamamoto, K. Mizunuma, H. Gan, M. Endo, S. Kanai, J. Hayakawa, F. Matsukura, and H. Ohno, *Nature materials* **9**, 721 (2010).
- [7] A. Brataas, A. D. Kent, and H. Ohno, *Nature materials* **11**, 372 (2012).
- [8] W.-G. Wang, M. Li, S. Hageman, and C. Chien, *Nature materials* **11**, 64 (2012).
- [9] J. Hayakawa, S. Ikeda, Y. M. Lee, F. Matsukura, and H. Ohno, *Applied Physics Letters* **89**, 232510 (2006).
- [10] Y. M. Lee, J. Hayakawa, S. Ikeda, F. Matsukura, and H. Ohno, *Applied Physics Letters* **90**, 212507 (2007).
- [11] S. Ikeda, J. Hayakawa, Y. Ashizawa, Y. M. Lee, K. Miura, H. Hasegawa, M. Tsunoda, F. Matsukura, and H. Ohno, *Applied Physics Letters* **93**, 082508 (2008).
- [12] S. Kamali, C. L. Zha, Y. Yoda, and J. Åkerman, *Journal of Physics: Condensed Matter* **25**, 135302 (2013).
- [13] S. Kamali, C. L. Zha, Y. Yoda, and J. Åkerman, *Journal of Physics: Condensed Matter* **26**, 026004 (2013).
- [14] J. J. Cha, J. C. Read, W. F. Egelhoff, P. Y. Huang, H. W. Tseng, Y. Li, R. A. Buhrman, and D. A. Muller, *Applied Physics Letters* **95**, 032506 (2009).
- [15] X. Kozina, S. Ouardi, B. Balke, G. Stryganyuk, G. H. Fecher, C. Felser, S. Ikeda, H. Ohno, and E. Ikenaga, *Applied Physics Letters* **96**, 072105 (2010).
- [16] S. V. Karthik, Y. K. Takahashi, T. Ohkubo, K. Hono, H. D. Gan, S. Ikeda, and H. Ohno, *Journal of Applied Physics* **111**, 083922 (2012).
- [17] Y. Ivanisenko, C. Kübel, S. H. Nandam, C. Wang, X. Mu, O. Adjaoud, K. Albe, and H. Hahn, *Advanced Engineering Materials* **20**, 1800404 (2018).
- [18] P. Lamparter, W. Sperl, and S. Steeb, *Zeitschrift für Naturforschung A* **37**, 1223 (1982).
- [19] L. Pusztai and E. Sváb, *Journal of Physics: Condensed Matter* **5**, 8815 (1993).
- [20] X. Yue, A. Inoue, C.-T. Liu, and C. Fan, *Materials Research* **20**, 326 (2017).
- [21] M. Ghafari, S. Kohara, H. Hahn, H. Gleiter, T. Feng, R. Witte, and S. Kamali, *Applied Physics Letters* **100**, 133111 (2012).
- [22] M. Ghafari, H. Hahn, H. Gleiter, Y. Sakurai, M. Itou, and S. Kamali, *Applied Physics Letters* **101**, 243104 (2012).
- [23] S. J. Billinge, *Philosophical Transactions of the Royal Society A* **377**, 20180413 (2019).
- [24] T. E. Faber and J. M. Ziman, *The Philosophical Magazine: A Journal of Theoretical Experimental and Applied Physics* **11**, 153 (1965).
- [25] M. Harada, R. Ikegami, L. S. R. Kumara, S. Kohara, and O. Sakata, *RSC Adv.* **9**, 29511 (2019).
- [26] A. Guinier, *Physics Today* **22**, 25 (1969).
- [27] B. E. Warren, *x-ray diffraction* (Dover publications, Inc., New York, USA, 1969).
- [28] T. Egami and S. Billinge, *Underneath the Bragg Peaks: Structural Analysis of Complex Materials* (Pergamon Press, Oxford, UK, 2003).
- [29] S. J. L. Billinge and I. Levin, *Science* **316**, 561 (2007).
- [30] S. K. Pradhan, Z. T. Deng, F. Tang, C. Wang, Y. Ren, P. Moeck, and V. Petkov, *J. Appl. Phys.* **102**, 044304 (2007).
- [31] M. Fernández-García, C. Berver, J. C. Hanson, X. Wang, and J. A. Rodriguez, *J. Am. Chem. Soc.* **129**, 13604 (2007).
- [32] V. Petkov, *Materials Today* **11**, 28 (2008).
- [33] E. S. Bözin, C. D. Malliakas, P. Souvatzis, T. Profferi, N. A. Spaldin, M. G. Kanatzidis, and S. L. Billinge, *Science* **330**, 1660–1663 (2010).
- [34] K. M. Ø. Jensen, E. S. Bözin, C. D. Malliakas, M. B. Stone, M. D. Lumsden, M. G. Kanatzidis, S. M. Shapiro, and S. J. L. Billinge, *Physical Review* **B86**, 085313 (2012).
- [35] D. A. Keen and A. L. Goodwin, *Nature* **521**, 303 (2015).
- [36] F. L. Deepak, M. Bañobre-López, E. Carbó-Argibay, M. F. Cerqueira, Y. Piñeiro-Redondo, J. Rivas, C. M. Thompson, S. Kamali, C. Rodríguez-Abreu, K. Kovnir, and Y. V. Kolen'ko, *The Journal of Physical Chemistry C* **119**, 11947 (2015).
- [37] A. Mancini and L. Malavasi, *Chem. Commun.* **51**, 16592 (2015).
- [38] K. M. Ø. Jensen, A. B. Blichfeld, S. R. Bauers, S. R. Wood, E. Dooryhee, D. C. Johnson, B. B. Iversen, and S. J. L. Billinge, *IUCrJ* **2**, 481–489 (2015).
- [39] K. M. Jensen, P. Juhas, M. A. Tofanelli, C. L. Heinecke, G. Vaughan, C. J. Ackerson, and S. J. Billinge, *Nature Communications* **7**, 11859 (2016).
- [40] A.-C. Dippel, K. M. Ø. Jensen, C. Tyrsted, M. Bremholm, E. D. Bøjesen, D. Saha, S. Birgisson, M. Christensen, S. J. L. Billinge, and B. B. Iversen, *Acta Cryst.* **A72**, 645–650 (2016).
- [41] A.-C. Dippel, M. Roelsgaard, U. Boettger, T. Schneller, O. Gutowski, and U. Ruett, *IUCrJ* **6**, 290–298 (2019).
- [42] M. K. Mathiesen, R. Väli, M. Härmas, E. Lust, J. F. Bulow, K. M. Ø. Jensen, and P. Norby, *J. Mater. Chem. A* **7**, 11709 (2019).
- [43] T. L. Christiansen, E. D. Bøjesen, M. Juelsholt, J. Etheridge, and K. M. Ø. Jensen, *ACS Nano* **13**, 8725 (2019).
- [44] S. Banerjee, C.-H. Liu, K. M. Ø. Jensen, P. Juhas, J. D. Lee, M. Tofanelli, C. J. Ackerson, C. B. Murray, and S. J. L. Billinge, *Acta Cryst.* **A76**, 24 (2020).
- [45] T. L. Christiansen, S. R. Cooper, and K. M. Ø. Jensen, *Nanoscale Adv.* **2**, 2234 (2020).
- [46] K. Pussi, J. Gallo, K. Ohara, E. Carb-Argibay, Y. V. Koleńko, B. Barbiellini, A. Bansil, and S. Kamali, *Condens. Matter* **5(1)**, 19 (2020).
- [47] K. Pussi, B. Barbiellini, K. Ohara, E. Carbo-Argibay, Y. V. Kolen'ko, A. Bansil, and S. Kamali, *Journal of Physics: Condensed Matter* **32**, 485401 (2020).
- [48] K. Pussi, B. Barbiellini, K. Ohara, E. Carbo-Argibay, V. Sousa, Y. V. Kolen'ko, A. Bansil, and S. Kamali, "Structural properties of a nanometer-sized silicon supported gold particles thin film," (2020), submitted.
- [49] D. Li, J. Zhuang, T. Liu, Z. Lu, and S. Zhou, *Journal of Materials Processing Technology* **211**, 1764 (2011).
- [50] S. Kohara, M. Itou, K. Suzuya, Y. Inamura, Y. Sakurai, Y. Ohishi, and M. Takata, *Journal of Physics: Condensed Matter* **19**, 506101 (2007).
- [51] D. G. Quirinale, *Structural and magnetic properties of metastable phases and undercooled liquids in Fe₈₃B₁₇*, Ph.D. thesis (2017).
- [52] T. Egami, *Journal of Applied Physics* **50**, 1564 (1979).
- [53] P. Juhás, C. L. Farrow, X. Yang, K. R. Knox, and S. J. L. Billinge, *Acta Crystallogr. A* **71**, 562 (2015).
- [54] M. G. Tucker, D. A. Keen, M. T. Dove, A. L. Goodwin, and Q. Hui, *Journal of Physics: Condensed Matter* **19**, 335218 (2007).
- [55] T. E. Gorelik, R. Neder, M. W. Terban, Z. Lee, X. Mu, C. Jung, T. Jacob, and U. Kaiser, *Acta Crystallographica Section B* **75**, 532 (2019).
- [56] M. Imafuku, S. Sato, H. Koshiba, E. Matsubara, and A. Inoue, *Scripta Materialia* **44**, 2369 (2001).

- [57] M. Shapaan, J. Gubicza, J. Lendvai, and L. Varga, *Materials Science and Engineering: A* **375 - 377**, 785 (2004).
- [58] J. Long, P. R. Ohodnicki, D. E. Laughlin, M. E. McHenry, T. Ohkubo, and K. Hono, *Journal of Applied Physics* **101**, 09N114 (2007).
- [59] P. V. Paluskar, J. J. Attema, G. A. de Wijs, S. Fiddy, E. Snoeck, J. T. Kohlhepp, H. J. M. Swagten, R. A. de Groot, and B. Koopmans, *Phys. Rev. Lett.* **100**, 057205 (2008).
- [60] D. Kirk, A. Kohn, K. B. Borisenko, C. Lang, J. Schmalhorst, G. Reiss, and D. J. H. Cockayne, *Phys. Rev. B* **79**, 014203 (2009).
- [61] Z. H. Stachurski, *Materials (Basel, Switzerland)* **4**, 1564 (2011), 28824158[pmid].
- [62] S. X. Huang, T. Y. Chen, and C. L. Chien, *Applied Physics Letters* **92**, 242509 (2008).
- [63] J. Díaz, C. Quirós, L. M. Alvarez-Prado, C. Aroca, R. Ranchal, M. Ruffoni, and S. Pascarelli, *Phys. Rev. B* **85**, 134437 (2012).
- [64] C. Chien, D. Musser, E. Gyorgy, R. Sherwood, H. Chen, F. Luborsky, and J. Walter, *Physical Review B* **20**, 283 (1979).
- [65] J. R. Schneider and U. Ruett, “Condensed matter research with high-energy synchrotron radiation,” (2020).
- [66] H. Zhu, Y. Huang, J. Ren, B. Zhang, Y. Ke, A. K.-Y. Jen, Q. Zhang, X.-L. Wang, and Q. Liu, *Advanced Science* **8**, 2003534 (2021).
- [67] T. Lookman and P. Littlewood, *MRS bulletin* **34**, 822 (2009).